Research Article

Yue Huang*, Rolando V. Aguilar, Stuart A. Trugman, Sang-Wook Cheong, Yuan Long, Min-Cheol Lee, Jian-Xin Zhu, Priscila F.S. Rosa, Rohit P. Prasankumar, Dmitry A. Yarotski, Abul Azad, Nicholas S. Sirica and Antoinette J. Taylor

Electrodynamics of photo-carriers in multiferroic $Eu_{0.75}Y_{0.25}MnO_3$

https://doi.org/10.1515/nanoph-2024-0641
Received November 15, 2024; accepted January 16, 2025; published online February 10, 2025

Abstract: Understanding and controlling the antiferromagnetic order in multiferroic materials on an ultrafast time scale is a long standing area of interest, due to their potential applications in spintronics and ultrafast magnetoelectric switching. We present an optical pump-terahertz (THz) probe study on multiferroic $Eu_{0.75}Y_{0.25}MnO_3$. The optical pump predominantly excites the d-d transitions of the Mn^{3+} ions, and the temporal evolution of the pump-induced transient conductivity is measured with a subsequent THz pulse. Two distinct, temperature-dependent decay times are revealed. The shorter relaxation time corresponds to spin-lattice thermalization, while the longer one is ascribed to electron-hole recombination. A spin-selection rule in the relaxation process is proposed in the magnetic phase. Slight suppression of the electromagnons was observed after the optical pump pulse within the spin-lattice thermalization time scale. These observed fundamental magnetic processes can shed light on ultrafast control of magnetism and photoinduced phase transitions in multiferroics.

Keywords: ultrafast spectroscopy; multiferroics; electromagnon dynamics; terahertz

***Corresponding author: Yue Huang**, Center for Integrated Nanotechnologies, Los Alamos National Laboratory, Los Alamos, NM 87545, USA, E-mail: yhuang@lanl.gov. https://orcid.org/0000-0002-2326-5605
Rolando V. Aguilar, **Stuart A. Trugman**, **Yuan Long**, **Min-Cheol Lee**, **Jian-Xin Zhu**, **Priscila F.S. Rosa**, **Dmitry A. Yarotski**, **Abul Azad and Antoinette J. Taylor**, Center for Integrated Nanotechnologies, Los Alamos National Laboratory, Los Alamos, NM 87545, USA
Sang-Wook Cheong, Rutgers Center for Emergent Materials and Department of Physics and Astronomy, Rutgers University, Piscataway, NJ, 08854, USA
Rohit P. Prasankumar, Enterprise Science Fund, Intellectual Ventures, Bellevue, WA, 98005, USA
Nicholas S. Sirica, Center for Integrated Nanotechnologies, Los Alamos National Laboratory, Los Alamos, NM 87545, USA; and U.S. Naval Research Laboratory, Washington, DC 20375, USA

1 Introduction

The coexistence of electric and magnetic order in multiferroics has made these materials the subject of intense investigation, due to the possibility of indirectly manipulating charge, spin, and orbital degrees of freedom by exploiting the strong coupling between these various quantities [1]–[5]. Such coupling between ferroic orders has a clear technological appeal, as the interplay between e.g. ferroelectric and ferromagnetic order can be used to electronically (magnetically) manipulate the magnetic (electronic) state for memory storage applications [6], [7]. The relative coupling strength between these ferroic orders is dependent on their material class [8]. For type I multiferroics, the noncentrosymmetric lattice distortion responsible for driving ferroelectric order occurs independent of magnetic order, whereas many type II multiferroics show ferroelectricity that is induced by exchange striction in the magnetically ordered state. In the latter case, polar lattice distortions lower the energy of the antisymmetric Dzyaloshinskii–Moriya exchange interaction, leading to a net electric polarization that develops in the noncollinear, spiral spin state [9]–[11]. Such strong magnetoelectric coupling in type II multiferroics demonstrates how frustrated magnetic exchange and non-collinear spin order go hand in hand with competing exchange processes to produce ferroelectricity.

Coupling between low lying lattice and magnetic excitations in multiferroics results in a spin wave that interacts strongly with light by acquiring electric dipole activity from infrared active phonons [12], [13]. The origin of this so-called electromagnon is contested, with initial claims arguing that the same magnetoelectric coupling responsible for the emergence of ferroelectricity in the spin spiral state gives rise to the electromagnon. In this case long-wavelength fluctuations of the polarization develop in response to cycloidal spin order [7], [13]. However, selection rules predicted by this mechanism are inconsistent with polarization-dependent infrared absorption, leading to an

alternate description rooted in spin-lattice coupling and shown to be fully consistent with a symmetric Heisenberg exchange model [14]. Regardless of origin, non-resonant optical excitation provides a promising route to modify electromagnons through both disrupting long-range magnetic order [15], [16], and generating photoexcited carriers capable of screening the electric polarization [17], [18]. The slight suppression and subsequent recovery of the electromagnon can be investigated on the intrinsic timescale of spin-lattice relaxation, allowing for new insights into magnetoelectric coupling.

In this manuscript, we describe optical pump – terahertz (THz) probe (OPTP) experiments on the rare-earth manganite $Eu_{0.75}Y_{0.25}MnO_3$ (EYMO). Like other perovskite manganites ($RMnO_3$; R = Gd, Dy, Tb) [19], [20], EYMO exhibits a range of magnetic and polar phases, but lacks any interference arising from the magnetic contribution of $4f$ moments [21]. Here, Jahn-Teller active, Mn^{3+} ions sit at the center of corner-sharing octahedra and undergo an orthorhombic lattice distortion brought on by the isovalent substitution of Y for Eu, enabling quasi-continuous tuning of the average rare-earth ionic radii [21]. The increased crystalline disorder brought on by such distortions leads to magnetic frustration, where a strong competition between ferromagnetic nearest neighbor (NN) and antiferromagnetic next nearest neighbor (NNN) superexchange results in collinear sinusoidal magnetic order in the ab-plane for $T < T_N = 47$ K [22], [23]. At $T = 30$ K, an electric polarization develops in the ac-plane ($P_a \gg P_c$) as a consequence of this magnetic order, leading to the emergence of two electromagnon excitations at THz frequencies ($E_{THz} \| a$-axis) [13], [24]. While generally robust against an above-gap optical excitation at the $h\nu = 1.55$ eV resonance of Mn intersite d-d transitions, we demonstrate here a reduction of the electromagnon on a timescale consistent with spin-lattice thermalization [25], [26]. Together with the opening of a new relaxation channel in the OPTP response for $T < T_N$, our results reveal how collective modes in this prototypical type II multiferroic compound are influenced by optical excitations possessing a characteristically larger energy scale.

2 Experiment and results

OPTP experiments were performed with an amplified Ti:Sapphire laser system operating at a 1 KHz repetition rate. Ultrashort optical pulses ($E = 3.5$ mJ; $\Delta t < 35$ fs) centered at 800 nm (1.55 eV) were split into three beams (50:40:10) and used for pump excitation, THz generation and electro-optic detection, respectively. Broadband (0.1–2.5 THz) THz pulses generated by optical rectification in (110) ZnTe were polarized parallel to the crystallographic a-axis of a 20 μm thick (001) EYMO ($x = 0.25$) single crystal polished to <0.5 μm roughness and attached to a high-resistivity Si wafer. Transmitted THz from both EYMO as well as a high-resistivity Si reference were detected by free space electro-optic sampling using in a 0.5 mm thick ZnTe crystal, with the entirety of the THz path purged by dry air (<3 %) to mitigate the effect of water absorption. Near normally incident optical pulses with a moderate pump fluence of <4 μJ/cm^2 were used to avoid saturation in the photoinduced response, while ensuring a reasonable signal-to-noise ratio. Finally, all experiments were carried out in an optical cryostat ($T < 10$ K), allowing for the determination of the complex refractive index $\tilde{n}(\omega) = n(\omega) + ik(\omega)$ in the multiferroic phase of EYMO through use of an optical cavity model [27]:

$$n(\omega) = 1 - \frac{c}{\omega d} \times \mathrm{Im}(T_r) \quad (1)$$

$$k(\omega) = -\frac{c}{\omega d}\{\ln \mathrm{Re}(T_r) + \ln \frac{(n_r + n(\omega))(1 + n(\omega))}{2(1 + n_r)n(\omega)}\} \quad (2)$$

Here c is the velocity of light, d is the thickness of the sample, n_r is the refractive index of the reference, and ω is the frequency. $\mathrm{Re}(T_r)$ and $\mathrm{Im}(T_r)$ are the real and imaginary parts of the transmission, respectively.

Figure 1a shows the change of the electric field ΔE at different delay times. $\Delta E(t, t_p)$ is measured by placing the chopper in the optical pump beam and scanning the THz gate line. We can expect $E_{\mathrm{sam}}(t, t_p) = E_{\mathrm{sam}} + \Delta E(t, t_p)$ [28] (E_{sam} is the transmitted THz electric field without optical pump), and calculate the transient transmission accordingly. The inset of Figure 1a shows the transmitted THz trace through our EYMO sample at 10 K (black, left axis) prior to pump excitation. With optical pumping, a reduction of the transmitted THz electric field by 0.2 % at $\Delta t = 46$ ps can be isolated through depicting the photoinduced change ΔE as measured across the entire trace (blue, right axis). The complex refractive index deduced from Eq. (1) and (2) allows for both the THz transmission function and the real part of the optical conductivity, $\sigma_1(\omega)$, to be computed for our EYMO sample in the multiferroic phase (T = 10 K) as a function of pump delay (Figure 1b). In the absence of pump excitation, the inset of Figure 1b reveals two local minima in the transmission at 0.7 THz (2.9 meV) and 2.4 THz (10 meV). Such features manifest as a respective peak and shoulder in $\sigma_1(\omega)$, corresponding to the two electromagnon modes observed from infrared reflectivity [13]. Following optical excitation, there is an increase of spectral weight in $\sigma_1(\omega, \Delta t)$ below 1.25 THz, which progressively recedes for longer pump-probe delays. By taking the difference in the transient conductivity, $\Delta\sigma_1(\omega) = \sigma_1(\omega, \Delta t) - \sigma_1(\omega, 0)$ in Figure 1c, a local reduce at the electromagnon energies is

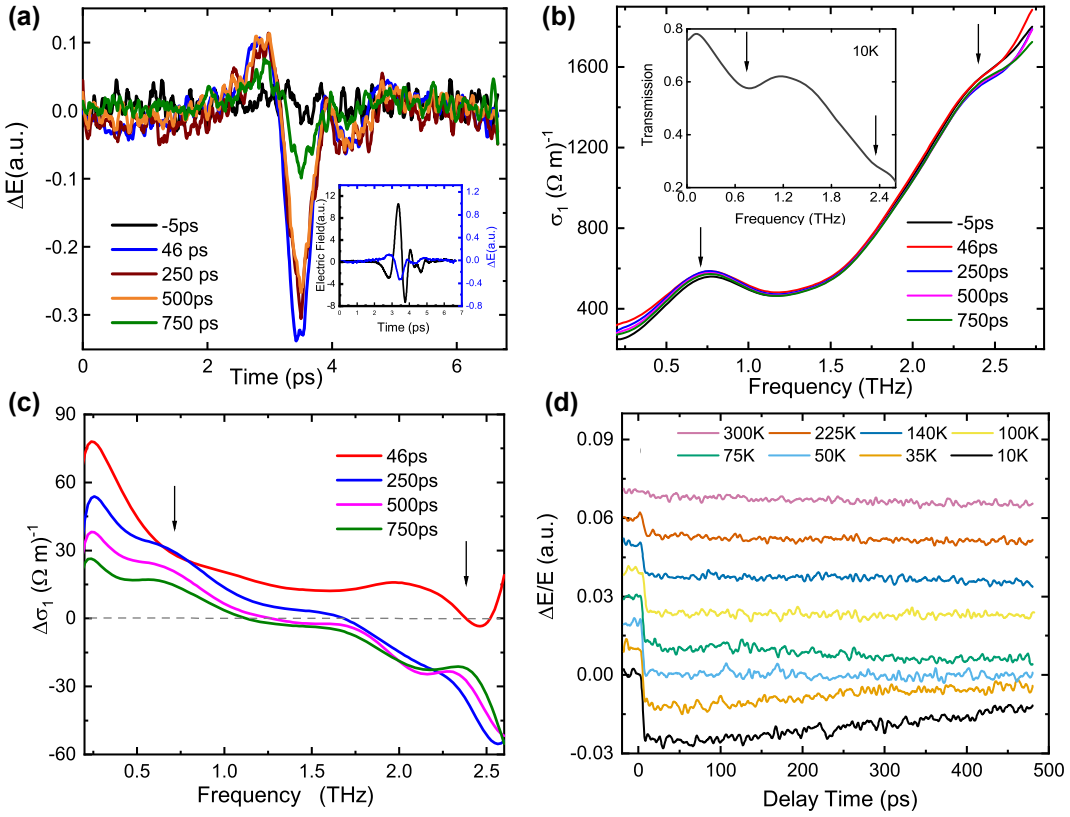

Figure 1: (Color online) (a) optical pump-induced change in THz field at different time delay. Inset: Time domain THz electric field transmitted through the sample without pump light (black, left axis). The difference between the THz electric field ΔE with and without the pump at 46 ps (blue, right axis, ×10). (b) The transient conductivity at different delay time. Inset: the transmission without pump. The arrows indicate the electromagnons. (c) The difference between conductivity with and without pump at the different delay times. All the above measurements in a,b, and c are taken at 10 K. (d) The frequency-integrated response of the 800-nm pump-THz probe signal at various temperatures: ΔE.

observed at a delay time of 46 ps which recovers at much longer delays (>250 ps), with the screening of the enhancement of the conductivity from photo-excited carrier at the low frequency.

Figure 1d shows the temperature dependence of the frequency-integrated pump-probe signal at the THz peak position versus delay time. For better visualization, the data at different temperatures are offset by 0.01 along the y-axis. The photoinduced change of transmission $\Delta E/E$ is negative which is attributed to photoexcitation of itinerant carriers following the pump excitation, and is consistent with the positive $\Delta\sigma_1(\omega)$ observed in Figure 1c. At high temperatures in the paramagnetic phase ($T > 47$ K), the transmission decreases abruptly following the arrival of the pump pulse, and the decrease in transmission magnitude can remain unchanged for several nanoseconds. Two additional features emerge below T_N: the initial fast decay time increases significantly with decreasing temperature and we observe a faster recovery time of the photoinduced change in $\Delta E/E$. We fit our differential transmission signal using bi-exponential decay function $A_1 * \exp(t/\tau_1) + A_2 * \exp(t/\tau_2)$. Assuming the probe pulse has a Gaussian profile with width γ, the convolution of the signal and probe pulse leads to the final fit function, as described in Equation (3):

$$\Delta E/E(t) = C + A_1 \exp\left(\frac{\gamma^2 - 2t\tau_1}{2\tau_1^2}\right)\left\{1 + erf\left(\frac{-\gamma^2 + t\tau_1}{\sqrt{2}\tau_1\gamma}\right)\right\} + A_2 \exp\left(\frac{\gamma^2 - 2t\tau_2}{2\tau_2^2}\right)\left\{1 + erf\left(\frac{-\gamma^2 + t\tau_2}{\sqrt{2}\tau_2\gamma}\right)\right. \quad (3)$$

The first exponential term describes the initial fast decrease in $\Delta E/E$, while the second term accounts for the recovery. The erf function is the convolution of the temporal evolution of each process with the decay and probe autocorrelation functions. In the paramagnetic phase, the recovery time extends to >10 ns, so we set τ_2 to infinity in the equation by using a constant C instead of the second term to fit the high temperature data. The results of this fit

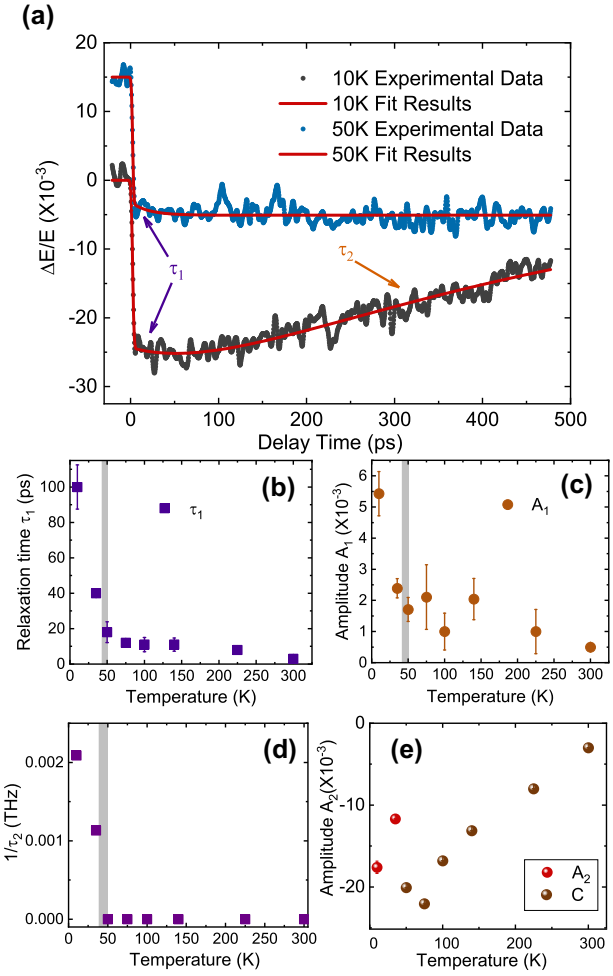

Figure 2: (Color online) (a) Frequency-integrated pump-probe versus delay time at 10 K and 50 K (black and blue dots; offset 0.015 along the *y*-axis from the original data). Red curve, fit to the data using the function in Eq. (3). Arrows and labels pointing to the parameters in Eq.(3): the long-rise dynamics represented by τ_1 and the slow dynamics by τ_2. (b) and (c) Temperature dependence of the fit parameter for τ_1 and amplitude A_1. (d) Temperature dependence of $1/\tau_2$. (e) The amplitude A_2 and constant C. For (b), (c) and (d) the grey line marks T_N.

at 10 K and 50 K are presented in Figure 2a. The initial decay time τ_1 and amplitude A_1, represented by the first term in equation (3), increase slowly as the temperature decreases in the paramagnetic phases and then abruptly below T_N (47 K), as displayed in Figure 2b and c. Next, we consider the recovery dynamics for $\Delta E/E$. As shown in Figure 2a, the dynamics fits well to two exponential functions below T_N, while above T_N the recovery extends to nanoseconds, beyond the time window of our measurement and hence we fit the dynamics with a constant C. We therefore plot $1/\tau_2$ versus temperature in Figure 2d. Figure 2e shows both the amplitude A_2 below T_N and constant C above T_N.

3 Discussion

Excitation by the 1.55eV pump pulse creates a population of hot carriers. Subsequently, the system undergoes thermalization via electron-electron ($e-e$) interactions, after which the energy is exchanged among lattice, orbital, and spin degrees of freedom. Processes involving electron-electron and electron–phonon coupling occur in on a picosecond timescale and cannot be resolved using our OPTP measurements. Therefore, we do not consider these processes in our analysis.

First, we consider the process driving the initial fast decrease in the transmission of $\Delta E/E$. We attribute this process, corresponding to τ_1 and A_1, to spin-lattice thermalization for the following reasons. Raman and FTIR studies on EYMO have revealed that the phonons exhibit temperature dependencies analogous to those of τ_1 and A_1. Raman measurements have shown that several phonons begin to soften at 100 K and continue this trend down to low temperatures [29]. FTIR measurements have revealed that the optical spectral weight of phonons shifts to lower energy as the temperature decreases [13]. In both cases, the temperature dependence is attributed to the strong spin-phonon coupling inherent to magnetic materials, and the magnitude of the change in A_1 is governed by the strength of the spin correlations. Further, the previous optical pump-probe measurements on $Eu_{0.75}Y_{0.25}MnO_3$ detected a spin-lattice relaxation time of 90 ps with a similar temperature dependence to our measurements of τ_1 [25]. This spin-lattice relaxation time was also observed in other magnetic insulators such as $TbMnO_3$, $HoMnO_3$, and $GdTiO_3$ using time-resolved THz and MOKE measurements [30]–[33]. Below T_N following optical excitation, energy is transferred from the phonons to spins and the antiferromagnetic (AFM) magnetic order is disrupted, requiring a longer time for the system to return to equilibrium and a corresponding larger amplitude of the photoinduced response. Both parameters dramatically increase as the temperature is lowered. The temperature dependence and scaling of τ_1 and A_1 behavior are sensitive to the onset of magnetic order, suggesting that τ_1 corresponds to the timescale for spin-lattice thermalization.

Next, we consider the recovery dynamics for $\Delta E/E$, with τ_2, A_2, and C plotted in Figure 2d and e. The comparable magnitudes of A_2 and C suggest that the same process drives the recovery in both the paramagnetic and magnetic phases, which we attribute to electron-hole (e-h) recombination. τ_2 is sub-nanosecond, in the magnetic phase, and increases to >10 ns in the paramagnetic phase, consistent with the typical timescale of e-h recombination [34]. At 10 K,

the transient low-frequency conductivity at 0.5 THz, which reflects the free carrier response, peaks at 46 ps and then decreases rapidly at longer delays, as shown in Figure 1c. The reduction of the low frequency conductivity spectral weight results from the lower free carrier density caused by e-h recombination. The trend of this reduction in the low-frequency spectral weight is consistent with the value of τ_2. At higher temperatures, e-h thermalization can be considerably prolonged, consistent with the observed several nanosecond relaxation time. In general, the e-h relaxation does not exhibit a marked temperature dependence in semiconductors [34]. Here the pronounced correlation of the decrease of τ_2 with the AFM phase transition suggests the opening of a new relaxation channel in the spin-ordered state.

To understand the temperature dependence of τ_2, we should consider the charge transfer process. The optical conductivity shows one broad absorption at 2 eV in stoichiometric rare-earth perovskite manganites, superimposed with several smaller spectral features [35], [36]. These low energy features correspond to intersite transitions of the $d_i^4 d_j^4$ to $d_i^3 d_j^5$ [35]–[37],as shown in Figure 3a. There are five possible final state configurations: a high spin (HS) state $^6A_1$ symmetry at the energy $U^* - 3J_H + \Delta_{JT}$, and four low spin states: $^4A_1$, $^4E_\epsilon$, $^4E_\theta$, $^4A_2$. Here U^* is the effective Coulomb repulsion on the same e_g orbital, J_H is the Hund interaction, and Δ_{JT} is the Jahn-Teller splitting of the e_g levels. In contrast to the paramagnetic state, both bi-collinear or cycloidal spin alignments in the antiferromagnetic state favor HS charge transfer in the *ab* plane with similar spin orientation and suppresses them along *c* axis [35]. The electrons and holes of the HS states below T_N preferentially recombine with those of similar spin orientation in the *ab* plane with a higher efficiency than random recombination in the paramagnetic state. Additionally, in the AFM state, recombination between sites with different orientations such as the opposite spin in the bi-collinear magnetic state or along the *c* axis is suppressed. The recombination process is displayed in Figure 3b, with the solid line indicating the preferred process and the dotted line for unfavorable charge transfer in the different magnetic phases. This scenario explains the strong temperature dependence of τ_2 we detected: the recombination relaxation time became much faster in the magnetically ordered states. We also fit the slower relaxation time (τ_2) with a power law function, and obtained the similar relaxation time as that derived from the exponential function. This further supports the τ_2 results from electron-holes recombination. The opening of a new channel of faster relaxation time below T_N is also observed in $GdTiO_3$ and

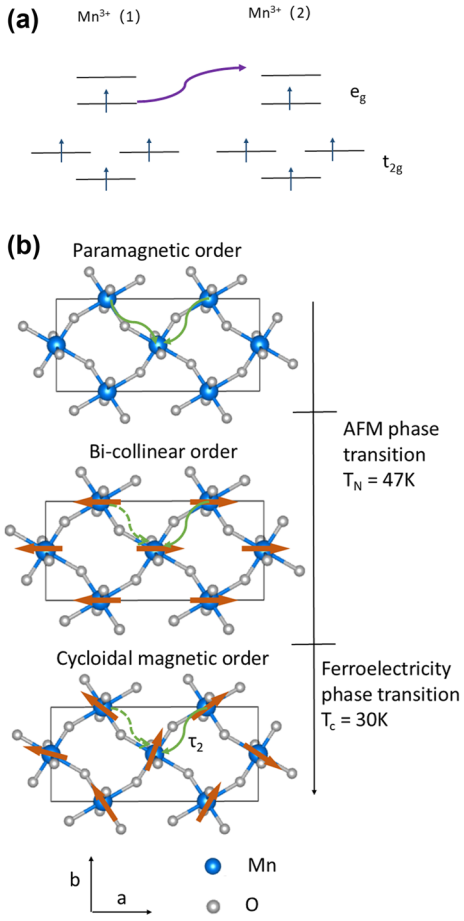

Figure 3: (Color online) (a) Optical transitions induced by the 800 nm pump. Absorption of a 1.55 eV photon creates a pair of Mn^{2+} and Mn^{4+}. (b) Schematic illustration of electron and hole recombination after the 1.55 eV laser excitation in different magnetic phases (Eu and Y atoms are omitted). The orange arrow on each Mn site depicts the spin orientation. The solid arrows represents the favored recombination process and the dotted lines indicate disfavored process.

$HoMnO_3$ compounds [30], [32], but has not been discussed in detail previously.

To delve further into the evolution of photoexcited itinerant carriers and electromagnon excitation, a Drude–Lorentz model was employed to describe the dielectric function:

$$\epsilon(\omega) = \epsilon_\infty - \frac{\omega_p^2}{\omega^2 + i\omega/\tau_D} + \sum_{i=1}^{N} \frac{S_i^2}{\omega_i^2 - \omega^2 - i\omega/\tau_i} \qquad (4)$$

The first term is the Drude component depicting the free carrier response, while the second term is the Lorentz components characterizing the electromagnon. ϵ_∞ is the dielectric constant at high frequencies. ω_p is the plasma frequency and τ_D ($1/\gamma_D$) is the free carrier lifetime. S_i is the

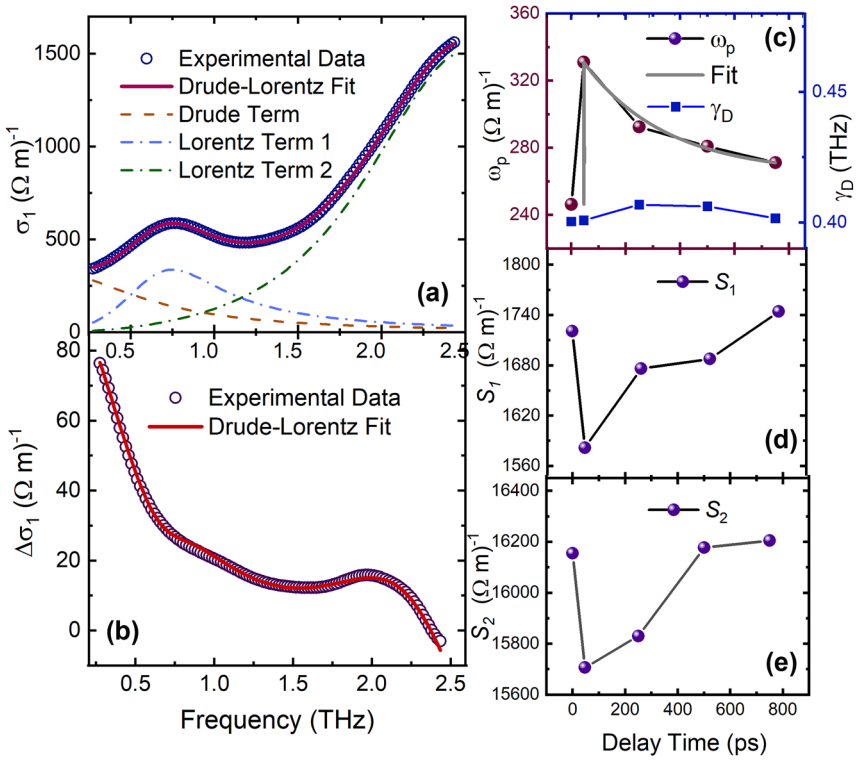

Figure 4: (Color online) (a) The blue circles are the transient optical real conductivity at 46 ps at 10 K. The solid curve is the Drude–Lorentz fit to the experimental data. (b) The red circles are the difference of the transient conductivity $\Delta\Sigma_1(t = 46\text{ ps}) = \Sigma_1(t = 46\text{ ps}) - \Sigma_1(t = 0\text{ ps})$. The solid curve are fit results of the experimental data. (c) Drude component of the photoexcited free carriers response: Delay time dependence of plasma frequency ω_p (right axis) and scattering rate $\gamma_D = 1/\tau_D$ at 10 K. The grey line shows the one term exponential function fit of ω_p. (d and e) Lorentz component: delay time dependence of S_1 and S_2.

square root of the oscillator strength and the ω_i is the resonance frequency of Lorentz components. The model was found to reproduce the conductivity spectrum, as shown in Figure 4a and b. All fitting parameters are displayed in Table 1.

Figure 4c shows the fit parameters of plasma frequency ω_p (left axis) and scattering rate (right axis) of the Drude term versus time delay. ω_p rises initially following optical excitation, and then decreases with the delay time. According to the Drude model, the square of ω_p is proportional to the effective carrier density n/m^* (where m^* is the effective carrier mass). The photoexcited charge carrier density is calculated as 1.1×10^{-5} per unit cell through the above relationship. Alternatively, the carrier density can also be estimated through the penetration depth. Considering a illumination of 1.55 eV light with a fluence of $F = 4\ \mu J/cm^2$, the penetration depth is 6.7×10^{-7} m according to the absorption spectrum of EYMO [24], and the charge carrier density is calculated as 5.8×10^{-5} per unit cell. The estimate of carrier density from the penetration depth is larger than the value from the Drude model, because only free carriers possessing high mobility contribute to the Drude response, whereas carriers with low mobility only contribute to the penetration depth. The ratio of these two values is around 0.2, suggesting that the carriers are excited into multiple bands and only a small fraction of them are photoexcited in the high mobility band. The transition at 1.5 eV occurs between the lower Hubbard band below the Fermi level and the upper Hubbard band. The conduction bands are more complex than a simple single-band mobility. In contrast to ω_p, the scattering rate, γ_D, does not exhibit a strong time dependence, indicating that the scattering

Table 1: The plasma frequency ω_p ($\Omega^{-1}m^{-1}$) and scattering rate $\gamma_D = 1/\tau_D$ (THz) for the Drude term, the resonance frequency ω_i (THz), the width $\gamma_i = 1/\tau_i$ (THz) and the square root of the oscillator strength S_i ($\Omega^{-1}m^{-1}$) for the Lorentz component for different time delays.

Time	ω_p	γ_D	ω_1	γ_1	S_1	ω_2	γ_2	S_2
−5 ps	246	0.4	0.74	0.471	1,721	2.46	1.05	16,154
46 ps	328	0.401	0.75	0.470	1,581	2.44	1.03	15,706
250 ps	296	0.406	0.75	0.471	1,676	2.46	1.06	15,830
500 ps	278	0.406	0.74	0.470	1,687	2.47	1.073	16,177
750 ps	272	0.401	0.74	0.472	1,744	2.48	1.076	16,205

rate remains unaffected as the electrons relax back to the valence band. Additionally, γ_D is significantly slower than in conventional semiconductors. This reduced scattering rate could result from the magnetic order of the material, which suppresses scattering pathways, or it could be attributed to the electronic band into which the electrons are excited. Specifically, the upper Hubbard band in doped EYMO may contribute to this behavior due to its intrinsic electronic structure.

The plasma frequency decreases after 100 ps, showing a similar relaxation trend to τ_2 shown in Figure 4c. The fit of the decay of plasma frequency versus time with an exponential function results in a relaxation time of 350 ps which is comparable to the τ_2 at 10 K. Since the square of plasma frequency is proportional to the free carrier density, its decay shows a reduction of photo-excited carriers which is consistent with the e-h recombination rate, further supporting the interpretation of the recovery process corresponding to τ_2 as carrier recombination.

The two Lorentz terms in Eq.(4) capture the two electromagnon modes. For the lower-frequency electromagnon, the resonance frequency ω_1 is 0.74 THz corresponding to the electromagnon position reported previously [13], [24]. The peak width γ_1, 0.47 THz, describes the scattering rate of the excitation. Both parameters remain essentially constant following 800-nm pump excitation. However, S_1 drops by 8 % (as compared to the 1 % error level from the fitting process), and then recovers to the initial level after 200 ps, as shown in Figure 4d. The electromagnon at higher frequency shows a similar decay time dependence in Figure 4e, but the fit results may be affected by the phonon at 120 cm^{-1} (3.5 THz) which was reported in the previous optical conductivity study [13].

The oscillator strength S_i^2 links to the magnitude of the excitation, indicating the two electromagnon modes are affected. The $e_g - e_g$ hopping transfer arising from the 800-nm pump, will lead to a spin frustration which does not flip the spin (not observed in our experiments). This frustration would perturb the Hamiltonian corresponding to the electromagnon excitation, resulting in a weak suppression in the amplitude of the electromagnon excitation that can be detected as a decrease in S_i, but not a change in the electromagnon frequency, ω_i, consistent with our measurement. The reduction of the electromagnon modes occurs within the 100 ps spin-lattice relaxation time scale. Considering the strong Heisenberg exchange model [14], the AC electric field causes distortions of the Mn−O−Mn bond configuration based on the spin-lattice coupling. Meanwhile, the relaxation time to the unperturbed state of S_1 is <100 ps, consistent with the observation of the reduction at electromagnon frequencies in the transient conductivity only at 46 ps in Figure 1c. Therefore, the above strong Heisenberg exchange model explained our discovery that the timescale of the electronmagons suppression is within spin-lattice relaxation process.

4 Conclusions

To conclude, we performed an optical pump THz probe study on $Eu_{0.75}Y_{0.25}MnO_3$. Our measurements found two clear relaxation times: a sub-100 ps rise time due to spin-lattice relaxation and a much longer magnetic order-related recovery due to electron-hole recombination. The spin-lattice thermalization shows a power law relationship with temperature. The temperature dependence of the electron-hole recombination suggests a channel opening below the Neel temperature, shortening the recovery time. A spin-selection rule in the relaxation process was proposed. Given its significance in the ultrafast manipulation of magnetic materials, further investigation of this process is warranted. The slight suppression of the electromagnon only found within the spin-lattice thermalization time range is consistent with the origin of electromagnon based on a strong Heisenberg exchange model. Our measurements demonstrate an attractive method for tracking the dynamics of material properties by directly probing low energy excitations such as electromagnons, and offer a powerful approach for understanding the coupling between different degrees of freedom in strongly correlated materials.

Research funding: This work was supported by the U.S. Department of Energy (DOE) Office of Science, XFEL, under DE-SC0019126, and LANL LDRD Program. SWC was supported by the W. M. Keck foundation grant to the Keck Center for Quantum Magnetism at Rutgers University. The work was primarily performed at the Center for Integrated Nanotechnologies, a U.S. Department of Energy, Office of Basic Energy Sciences user facility. Los Alamos National Laboratory is operated by Triad National Security, LLC, for the National Nuclear Security Administration of U.S. Department of Energy (Contract No. 89233218CNA000001).

Author contributions: RVA, SWC, YH and PR performed experiments. YH, YL and MCL analyzed data. AA designed the optical spectroscopy setup. All the co-authors wrote the paper. All authors have accepted responsibility for the entire content of this manuscript and approved its submission.

Conflict of interest: Authors state no conflicts of interest.

Informed consent: Informed consent was obtained from all individuals included in this study.

Ethical approval: The conducted research is not related to either human or animals use.

Data availability: The datasets generated and/or analysed during the current study are available from the corresponding author upon reasonable request.

References

[1] Y. Tokura and N. Nagaosa, "Orbital physics in transition-metal oxides," *Science*, vol. 288, no. 5465, pp. 462—468, 2000.

[2] S. Dong, J. M. Liu, S. W. Cheong, and Z. Ren, "Multiferroic materials and magnetoelectric physics: Symmetry, entanglement, excitation, and topology," *Adv. Phys.*, vol. 64, nos. 5—6, pp. 519—626, 2015.

[3] S.-W. Cheong and M. Mostovoy, "Multiferroics: A magnetic twist for ferroelectricity," *Nat. Mater.*, vol. 6, no. 1, pp. 13—20, 2007.

[4] S. Ismail-Beigi, F. J. Walker, A. S. Disa, K. M. Rabe, and C. H. Ahn, "Picoscale materials engineering," *Nat. Rev. Mater.*, vol. 2, no. 11, pp. 1—17, 2017.

[5] N. A. Spaldin and R. Ramesh, "Advances in magnetoelectric multiferroics," *Nat. Mater.*, vol. 18, no. 3, pp. 203—212, 2019.

[6] T. Kimura, T. Goto, H. Shintani, K. Ishizaka, T.-H. Arima, and Y. Tokura, "Magnetic control of ferroelectric polarization," *Nature*, vol. 426, no. 6962, pp. 55—58, 2003.

[7] Y. Takahashi, R. Shimano, Y. Kaneko, H. Murakawa, and Y. Tokura, "Magnetoelectric resonance with electromagnons in a perovskite helimagnet," *Nat. Phys.*, vol. 8, no. 2, pp. 121—125, 2012.

[8] D. Khomskii, "Classifying multiferroics: Mechanisms and effects," *Phys*, vol. 2, p. 20, 2009.

[9] H. Katsura, N. Nagaosa, and A. V. Balatsky, "Spin current and magnetoelectric effect in noncollinear magnets," *Phys. Rev. Lett.*, vol. 95, no. 5, p. 057205, 2005.

[10] I. A. Sergienko and E. Dagotto, "Role of the Dzyaloshinskii-Moriya interaction in multiferroic perovskites," *Phys. Rev. B*, vol. 73, no. 9, p. 094434, 2006.

[11] M. Mostovoy, "Ferroelectricity in spiral magnets," *Phys. Rev. Lett.*, vol. 96, no. 6, p. 067601, 2006.

[12] H. Katsura, A. V. Balatsky, and N. Nagaosa, "Dynamical magnetoelectric coupling in helical magnets," *Phys. Rev. Lett.*, vol. 98, no. 2, p. 027203, 2007.

[13] R. Valdés Aguilar, A. B. Sushkov, C. L. Zhang, Y. J. Choi, S.-W. Cheong, and H. D. Drew, "Colossal magnon-phonon coupling in multiferroic $Eu_{0.75}Y_{0.25}MnO_3$," *Phys. Rev. B*, vol. 76, no. 6, p. 060404, 2007.

[14] R. Valdés Aguilar, *et al*., "Origin of electromagnon excitations in multiferroic $RMnO_3$," *Phys. Rev. Lett.*, vol. 102, no. 4, p. 047203, 2009.

[15] J. A. Johnson, *et al*., "Magnetic order dynamics in optically excited multiferroic $TbMnO_3$," *Phys. Rev. B*, vol. 92, no. 18, p. 184429, 2015.

[16] E. Baldini, *et al*., "Lattice-mediated magnetic order melting in $TbMnO_3$," *Phys. Rev. B*, vol. 97, no. 12, p. 125149, 2018.

[17] N. Nilforoushan, *et al*., "Photoinduced renormalization and electronic screening of quasi-two-dimensional Dirac states in $BaNiS_2$," *Phys. Rev. Res.*, vol. 2, no. 4, p. 043397, 2020.

[18] P. Sivarajah, *et al*., "THz-frequency magnon-phonon-polaritons in the collective strong-coupling regime," *J. Appl. Phys.*, vol. 125, no. 21, 2019, https://doi.org/10.1063/1.5083849.

[19] M. Li, H. Tan, and W. Duan, "Hexagonal rare-earth manganites and ferrites: A review of improper ferroelectricity," *Phys. Chem. Chem. Phys.*, vol. 22, no. 26, pp. 14415—14432, 2020.

[20] M. B. Salamon and M. Jaime, "The physics of manganites: Structure and transport," *Rev. Mod. Phys.*, vol. 73, no. 3, pp. 583—628, 2001.

[21] J. Hemberger, *et al*., "Multiferroic phases of $Eu_{1-x}Y_xMnO_3$," *Phys. Rev. B*, vol. 75, no. 3, p. 035118, 2007.

[22] Y. Yamasaki, S. Miyasaka, T. Goto, H. Sagayama, T. Arima, and Y. Tokura, "Ferroelectric phase transitions of 3 d-spin origin in $Eu_{1-x}Y_xMnO_3$," *Phys. Rev. B*, vol. 76, no. 18, p. 184418, 2007.

[23] T. Kimura, *et al*., "Distorted perovskite with eg_1 configuration as a frustrated spin system," *Phys. Rev. B*, vol. 68, no. 6, p. 060403, 2003.

[24] A. Pimenov, A. Loidl, A. A. Mukhin, V. D. Travkin, V. Yu Ivanov, and A. M. Balbashov, "Terahertz spectroscopy of electromagnons in $Eu_{1-x}Y_xMnO_3$," *Phys. Rev. B*, vol. 77, no. 1, p. 014438, 2008.

[25] D. Talbayev, *et al*., "Spin-dependent polaron formation dynamics in $Eu_{0.75}Y_{0.25}MnO_3$ probed by femtosecond pump-probe spectroscopy," *Phys. Rev. B*, vol. 91, no. 6, p. 064420, 2015.

[26] I. P. Handayani, *et al*., "Dynamics of photo-excited electrons in magnetically ordered $TbMnO_3$," *J. Phys.: Condens. Matter*, vol. 25, no. 11, p. 116007, 2013.

[27] W. Withayachumnankul and M. Naftaly, "Fundamentals of measurement in terahertz time-domain spectroscopy," *J. Infrared, Millim., Terahertz Waves*, vol. 35, pp. 610—637, 2014.

[28] R. D. Averitt and A. J. Taylor, "Ultrafast optical and far-infrared quasiparticle dynamics in correlated electron materials," *J. Phys.: Condens. Matter*, vol. 14, no. 50, pp. R1357—R1390, 2002.

[29] S. Issing, A. Pimenov, V. Yu Ivanov, A. A. Mukhin, and J. Geurts, "Composition-dependent spin-phonon coupling in mixed crystals of the multiferroic manganite $Eu_{1-x}Y_xMnO_3$ ($0 \leq x \leq 0.5$) studied by Raman spectroscopy," *Phys. Rev. B*, vol. 81, no. 2, p. 024304, 2010.

[30] P. Bowlan, *et al*., "Directly probing spin dynamics in insulating antiferromagnets using ultrashort terahertz pulses," *Phys. Rev. B*, vol. 94, no. 18, p. 184429, 2016.

[31] P. Bowlan, *et al*., "Probing ultrafast spin dynamics through a magnon resonance in the antiferromagnetic multiferroic $HoMnO_3$," *Phys. Rev. B*, vol. 94, no. 10, p. 100404, 2016.

[32] D. J. Lovinger, *et al*., "Magnetoelastic coupling to coherent acoustic phonon modes in the ferrimagnetic insulator $GdTiO_3$," *Phys. Rev. B*, vol. 102, no. 8, p. 085138, 2020.

[33] A. V. Kimel, R. V. Pisarev, J. Hohlfeld, and T. Rasing, "Quenching of the Antiferromagnetic Order in $FeBO_3$: Direct Optical Probing of the Phonon-Magnon Coupling," *Phys. Rev. Lett.*, vol. 89, no. 28, p. 287401, 2002.

[34] R. P. Prasankumar and A. J. Taylor, *Optical Techniques for Solid-State Materials Characterization*, Boca Raton, CRC Press, 2016.

[35] N. N. Kovaleva, *et al*., "Spin-controlled mott-hubbard bands in $LaMnO_3$ probed by optical ellipsometry," *Phys. Rev. Lett.*, vol. 93, no. 14, p. 147204, 2004.

[36] A. S. Moskvin, A. A. Makhnev, L. V. Nomerovannaya, N. N. Loshkareva, and A. M. Balbashov, "Interplay of p-d and d-d charge transfer transitions in rare-earth perovskite manganites," *Phys. Rev. B*, vol. 82, no. 3, p. 035106, 2010.

[37] M. W. Kim, P. Murugavel, S. Parashar, J. S. Lee, and T. W. Noh, "Origin of the 2eV peak in optical absorption spectra of $LaMnO_3$: An explanation based on the orbitally degenerate Hubbard model," *New J. Phys.*, vol. 6, no. 1, pp. 1—12, 2004.